



PAPER

A cell-based dosimetry model for radium-223 dichloride therapy using bone micro-CT images and GATE simulations

Gabriella M Pinto^{1,4}, Daniel A B Bonifacio², Lidia V de Sá², Luis Felipe C Lima¹, Igor F Vieira³ and Ricardo T Lopes¹¹ Nuclear Instrumentation Laboratory (PEN/COPPE), Federal University of Rio de Janeiro, Rio de Janeiro-RJ, Brazil² Department of Medical Physics, Institute of Radioprotection and Dosimetry (IRD/CNEN), Rio de Janeiro-RJ, Brazil³ Department of Imaging and Pathology, Nuclear Medicine and Molecular Imaging, University Hospital and KU Leuven, Herestraat 49, B-3000 Leuven, Belgium⁴ Author to whom any correspondence should be addressed.E-mail: gpinto@nuclear.ufrj.br**Keywords:** cell-based dosimetry, radium-223 therapy, skeletal dosimetry, fuzzy c-means clustering method**Abstract**

Dosimetry at the cellular level has outperformed macrodosimetry in terms of agreement with toxicity effects in clinical studies. This fact has encouraged dosimetry studies aiming to quantify the absorbed doses needed to reach radiotoxicity at the cellular level and to inform recommendations on the administration of radium-223. The aim of this work is to qualitatively and quantitatively evaluate the absorbed doses of radium-223 and the interactions of the doses at the cellular level. The analysis was performed by Monte Carlo simulations in GATE using micro-CT image of a mouse. Two physics lists available in the GATE code were tested. The influence of single and multiple scattering models on the absorbed dose distribution and number of particle hits was also studied. In addition, the fuzzy c-means clustering method was used for data segmentation. The segmentation method was suitable for these analyses, particularly given that it was unsupervised. There was no significant difference in the estimated absorbed dose between the two proposed physics lists. The absorbed dose values were not significantly influenced by scattering, although single scattering resulted in twice as many interactions as multiple scattering. The absorbed dose histogram at the voxel level shows heterogeneous absorbed dose values within each shell, but the observations from the graph of the medians were comparable to those in the literature. The interaction histogram indicates 10^4 events, although some voxels had no interactions with alpha particles. However, the voxels did not show absorbed doses capable of deterministic effects in the deepest part of the bone marrow. The absorbed dose distribution in images of mouse trabecular bone was compatible with simple geometric models, with absorbed doses capable of deterministic effects near the bone surface. The interaction distributions need to be correlated with *in vivo* studies for better interpretation.

1. Introduction

Radium dichloride ($^{223}\text{RaCl}_2$) was the first alpha-emitting radiopharmaceutical approved for clinical use in patients with castration-resistant prostate cancer, as well as those with evidence of bone metastases but without visceral disease (Kluetz *et al* 2014); this drug produces higher overall survival than placebo (Parker *et al* 2013) in addition to achieving local disease regression (Pacilio *et al* 2016). The recommended dose is 50 kBq/kg (Pandit-Taskar *et al* 2014) in six treatment cycles lasting four weeks each (Mínguez *et al* 2018a). In clinical samples, under 1% of patients presented grade 4 haematological toxicity, and approximately 2%–4% presented grade 3 toxicity for haemoglobin, platelets, neutrophils or leukocytes (Nilsson *et al* 2007). These toxicity rates were below the expected value, indicating that the mean absorbed dose may not be the correct parameter to use to measure toxicity (Hobbs *et al* 2012).

High alpha-particle LET (linear energy transfer) results in clinical advantages, increasing cellular damage by producing double-strand DNA breaks at high rates or making cellular repair mechanisms inefficient (Mínguez

et al 2018b). Cellular survival studies indicate that the alpha emitters can kill a malignant tumour cell with only a few particles hitting its nucleus (McDevitt *et al* 1998), depositing an absorbed dose of approximately 0.14 Gy per collision (Kassis 2002). Furthermore, since the range is approximately 10 cellular diameters, there is high specificity (Sgouros 2008, Sgouros *et al* 2010), which minimizes the effect on non-targeted cells and, as a consequence, restricts toxicity levels in the surrounding healthy tissue (Lien *et al* 2015). The 50% lethal dose (LD_{50}) for acute radium-223 toxicity remains to be determined. This fact is an indicator that toxicity depends much more on the microscopic distribution of the source than on the activity of the specific radioisotope (Larsen *et al* 2006).

Haematopoietic bone marrow irradiation is associated with a risk of leukaemia induction, and the endosteal region (a shell 50 μm from the bone surface) is particularly associated with the risk of bone cancer (ICRP 2008, 2015). Since bone turnover sites are the principal locations of skeletal metastases (Dant *et al* 2013), cell-based dosimetric analysis will be performed to investigate the toxicity of radium-223 in the bone marrow and its efficacy in the endosteal region.

At present, skeletal dosimetry is performed using computational models founded on 3D image-based models, such as the paired-image radiation transport (PIRT) model developed in the Bolch laboratory in the USA (Pafundi *et al* 2009, 2010, Hough *et al* 2011) and the systematic-periodic cluster (SPC) method from Kramer's laboratory in Brazil (Kramer *et al* 2006, 2007, 2009, 2012). These models and their extensions are used to calculate the fraction absorbed from alpha emitters in the skeletal tissues of human phantoms (Pafundi 2009, Geyer *et al* 2017a, 2017b).

HENRIKSEN *et al* (2003) developed a mouse trabecular bone model consisting of a solid matrix containing a high density of spherical bone marrow cavities with three distinct radii and the same surface/volume ratios as human bone according to International Commission on Radiological Protection (ICRP) Publication 70 (1995). Those researchers estimated the absorbed dose at the bone surface as 70 Gy, sparing the central region of the red bone marrow. Hobbs *et al* (2012) also developed a simplified bone marrow model analysing the toxicity of radium-223 at the cellular level, showing that an increase in the average absorbed dose from 1 to 20 Gy in the bone marrow cavity results in a slight rise in the toxicity potential. Despite using simple geometric models, the correlation of these studies (Henriksen *et al* 2003, Hobbs *et al* 2012) with toxicity studies (Nilsson *et al* 2005, 2007) is better than that of dose estimation through active bone marrow macrodosimetry (Lassmann and Nosske 2013).

In addition, previous studies (Henriksen *et al* 2003, Hobbs *et al* 2011) that calculated the absorbed dose of radium-223 at the cellular level did not analyse beta emissions. Some authors (Larsen *et al* 2006) mention that beta components are not expected to play a significant role in terms of toxicity at therapeutic doses. However, other authors (Gholami *et al* 2015) believe that the contribution of beta emission to the absorbed dose should be investigated, as the damage caused by beta particles could be significant and should be better addressed. Therefore, this study sought to investigate the contribution of beta emissions to the absorbed dose.

The fuzzy c-means (FCM) clustering method (Chuang *et al* 2006), a segmentation method that is applied in this dosimetry study, assigns to each voxel a probability of membership in each cluster centre. This approach can be very powerful compared to traditional hard-thresholded segmentation methods such as PIRT and SPC, where every point is assigned a crisp, exact label. Furthermore, the output from this method, as well as that from the method developed in this work, can be repurposed to classify new data according to the calculated clusters, facilitating learning transfer for the segmentation of new cases in the future.

As previous studies have not unified realistic geometry models of bone tissue and updated dosimetry analyses for alpha particles, the present work proposes a methodology based on micro-CT images segmented using FCM (Chuang *et al* 2006). The analysis comprised the calculation of the absorbed dose and the number of interactions at the voxel level using GATE (Geant4 Application for Tomographic Emission) (Sarrut *et al* 2014) radiation transport code, which provides a detailed description of the radium-223 decay chain.

2. Materials and methods

First, the physics processes and GATE parameters adopted in the simulation were validated by comparing the results of the simulation to the absorbed fraction (AF) obtained from a known model (Hobbs *et al* 2012). This model was also updated, following ICRP Publication 110 (ICRP 2008), for comparison purposes. Posteriorly, a micro-CT image of a bone sample was acquired, and a segmentation method was applied to a volume of interest (VOI) to define a shell representing the radioactive source location. The GATE tools used for cellular-level analysis were also discussed.

2.2. Simulations With the GATE Tool

Radium-223 absorbed dose distributions were simulated using GATE version 8.1, based on the Geant4 (Geometry And Tracking, version 10.4) framework (Sarrut *et al* 2014). Geant4 physics constructor classes are provided in GATE as reference physics lists. The physics lists *emstandard_opt3* and *emstandard_opt4* were evaluated in this work, since they provide high accuracy for electrons, hadrons and ion tracking. However, *emstandard_opt3*

loads the Standard model for all relevant electromagnetic processes (Costa *et al* 2015), while `emstandard_opt4` employs the most accurate Standard, Livermore and Penelope models (Matta *et al* 2016).

The influence of multiple and single Coulomb scattering on the absorbed dose distribution and number of particle hits was also studied. The hits are the Geant4 particle interaction histories occurring in the detector (Jan *et al* 2011). A hit represents a physical interaction of a track within a sensitive region of the detector. The sensitive region is used by GATE to collect information such as the energy, position and time of a step. A hit occurs each time a primary or secondary particle makes a step in a volume, with or without energy deposition (Sarrut *et al* 2014). Regarding the influence of the voxel effect on these estimates, the smaller the voxel size for the simulation with the Geant4 code, the more reproducible the simulated scenario is, according to the literature (Elbast *et al* 2012).

The GATE/Geant4 Radioactive Decay Module (RDM) simulates radioactive decay on a per-decay level (Hauf *et al* 2013a, 2013b), which means any direct decay emission is sampled by the algorithm. RDM is based on data taken from the evaluated nuclear structure data file (ENSDF) (Martin 2013). `G4RadioactiveDecay` and associated classes simulate the decay of radioactive nuclei by alpha, beta+, and beta-emission and by electron capture (EC) (Allison 2016). `G4PhotonEvaporation` class handles nuclear deexcitation (i.e. γ -rays and conversion electrons). Fluorescence emission is simulated by the `G4AtomicDeexcitation` class. RDM simulates the full decay chain and its associated decay emission.

Radium-223 decays to lead-207 via short-lived daughters (figure 1(a)), emitting alpha, beta-, and gamma particles with different energies and emission probabilities. The simulated fractions of alpha, beta- and gamma energy emitted from the full decay chain of radium-223 are 95.5%, 3.0%, and 1.5%, respectively. Figures 1(b)–(e), respectively, show the simulated energy spectra of beta-, gamma, alpha and recoil ion particles emitted from the radium-223 decay chain.

GATE/Geant4 tracks charged particles to the end of their range (Agostinelli *et al* 2003) unless a particle production threshold is properly set to avoid unnecessary computation time while maintaining the accuracy of the results (Costa *et al* 2017, Carvalho *et al* 2018). This threshold is defined as a range and is internally converted to an energy value according to the material and the particle. Therefore, a physics process does not produce particles whose ranges would be less than a user-defined value, known as the range cut-off. In this situation, the suppressed particles have their energies deposited during or at the end of the step. The range cut for photons is defined by the absorption length. The range cut-off is required by some processes, such as delta ray and bremsstrahlung production, to suppress the generation of large numbers of gammas and soft electrons. A range cut-off value of 100 nm was adopted for gamma emissions, electrons and positrons.

The GATE DoseActor tool was used to calculate the number of interactions, the energy and the absorbed dose in each voxel of the micro-CT image of the bone sample. The DoseActor stores the required information in a 3D image (or matrix) with the same voxel size as the bone image (Carvalho *et al* 2018), enabling fast visualization of the dose distribution.

2.3. Simulation validation

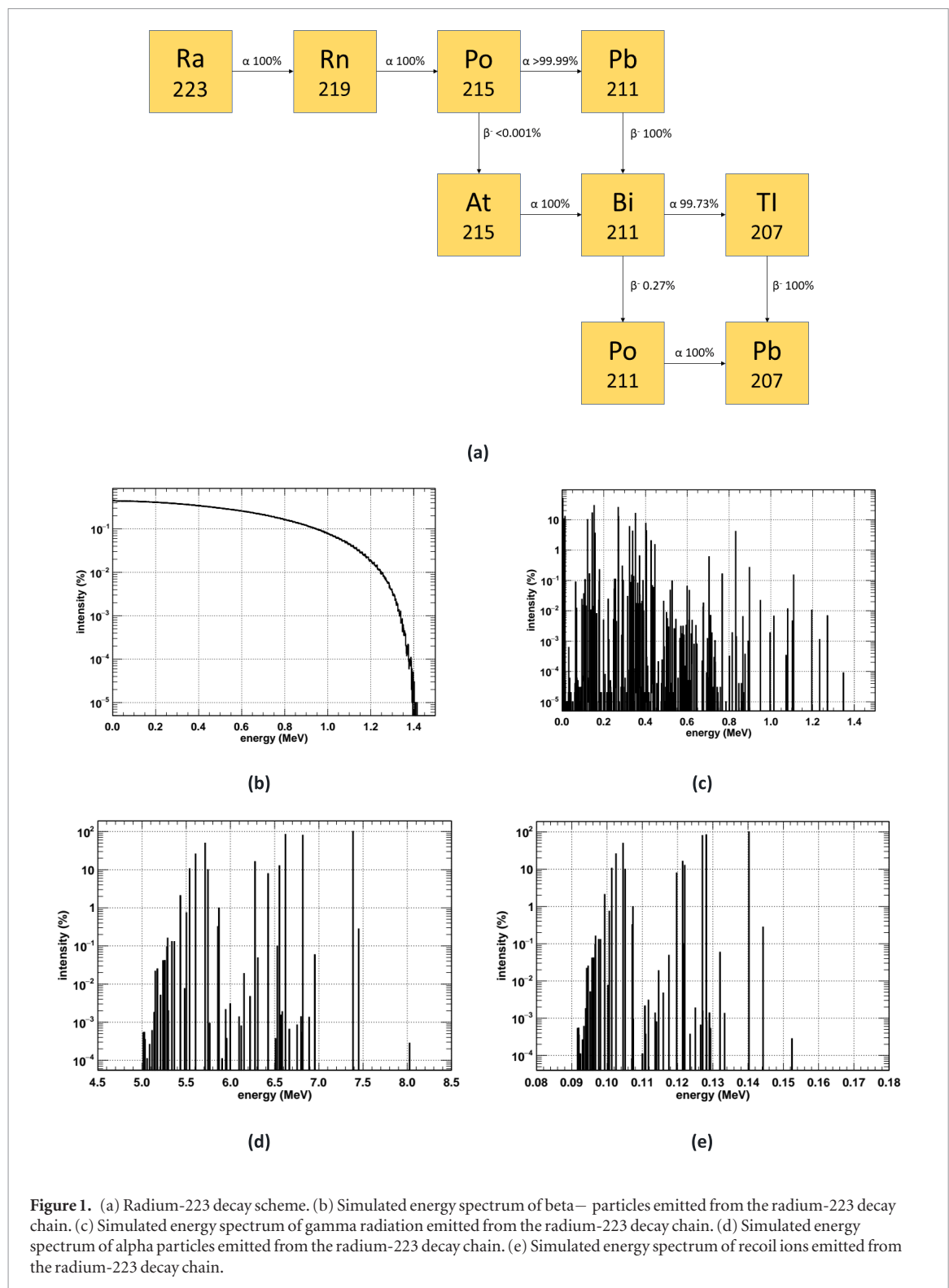
The simplified trabecular model from Hobbs *et al* (2012) was simulated with GATE for comparison purposes. The model consists of three concentric spherical layers representing the bone marrow, the endosteal region, and the trabecular bone, as shown in figure 2. The bone marrow was created as a 390 μm radius sphere; the endosteal region was represented by a spherical shell of radius 390 μm (internal) and 400 μm (external); and the trabecular region was created as another spherical shell with internal and external radii of 400 and 500 μm , respectively. The simulated source, located in the endosteal region, considers the entire radium-223 decay chain.

To validate the adopted simulation parameters, the AF values calculated with GATE were compared with the results from the Hobbs model, using 10^4 particles emitted.

The ICRP report 110 (2008) updated the endosteal region thickness value—previously given by the ICRP 30 (1979)—from 10 μm to 50 μm . Thus, this parameter was updated in the simplified model from Hobbs *et al* (2012) to determine the changes in the AF values. The source region, which was previously the endosteal layer, was restricted to a 10 μm -thick portion of the endosteal region nearest to the trabecular bone.

2.4. Bone sample

The pelvic region, the lumbar spine, the femur, and the thoracic spine are the most commonly affected regions in bone metastases from prostate cancer (Vieira *et al* 2012). The major challenge of cell-based dosimetry in the bone region is to reproduce the irregular geometry of these structures. In order to describe the geometry more realistically, micro-CT images of a bone sample were acquired for absorbed dose simulations in the bone structures. The selected sample was a femur from a healthy adult C57BL/6 mouse (figure 3) with a body weight of 23 g. The study was approved by the Ethics Committee on the Use of Animals (CEUA/UFRJ) with protocol number UFRJ-129/14. The mouse femur was chosen because its structures and the spatial gradient of its radiosensitive cells in the bone marrow cavity of the trabecular bone are similar to those of human femurs



(Watchman *et al* 2007). Moreover, the changes that occur in the bone structure during ageing are similar for adult mice and humans (Halloran *et al* 2002).

Femur imaging was performed immediately after the mouse was sacrificed. The image was acquired using a Bruker Skyscan 1173 micro-CT apparatus. The acquisition parameters are shown in table 1. No preservation technique was applied to the biological sample, and the soft tissue around the bone was dissected with a scalpel.

The image voxel size was $6.05 \times 6.05 \times 6.05 \mu\text{m}^3$, following the recommended voxel size ($<10 \mu\text{m}$) for an accurate trabecular microarchitecture analysis in mice (Van'tHof 2012). After reconstruction with the software *NRecon*, version 1.6.9.4, from *Bruker*, 2080 slices with a square matrix size of 1252 image pixels were obtained.

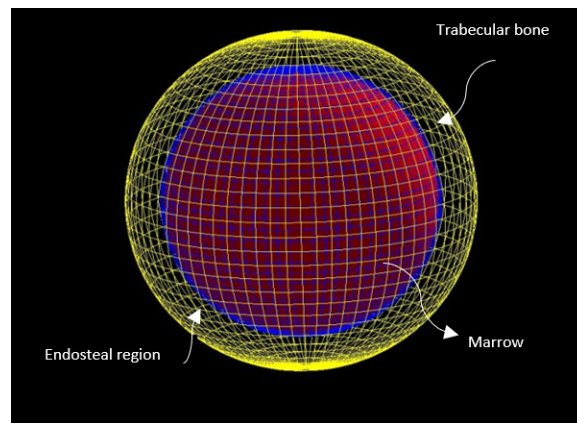


Figure 2. Representation of the simplified trabecular model from HOBBS *et al*, 2012 shown in the OGLIQt viewer of the GATE simulation code.

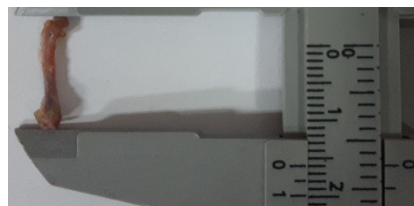


Figure 3. Picture of the scanned femur of a C57BL/6 mouse.

Table 1. Acquisition parameters for mouse femur imaging with micro-CT equipment.

Parameters	Value
Voltage	70 kV
Current	144 μ A
Rotation	0.5°
Pixel size	6.05 μ m
Matrix size	1252 \times 1252
Filter	1.0 mm Al

Figure 4 shows a 3D rendering of these slices reproduced by Avizo Fire (version 8.1, from Fei), a post-processing software.

Since the femur has different cellular distributions and geometries along the longitudinal axis (Lord 1990), this study evaluated a geometrically complex bone site, namely, the femoral neck. In addition to having a complex trabecular structure with a high rate of bone turnover, i.e. a preferential area for bone metastases, this region is also crucial from the dosimetric point of view, as it contains red bone marrow tissue in adults (Mitchell *et al* 1986, Valentin 2002).

2.5. Source location on the femur

Radium-223 assumes the function of the Ca^{+2} ion in the chemical reaction for the synthesis of hydroxyapatite by mature osteoblasts during the bone turnover process (Suominen *et al* 2017). Radium-223 adheres to the active bone formation areas found on healthy mineral bone matrices and bone metastases, which means that this radionuclide is not specific to malignant tumour cells, as shown in recent autoradiography studies with mice (Abou *et al* 2016, Suominen *et al* 2017).

The endosteum thickness was updated in ICRP Publication 110, but there is no mention of the change in the radium-223 uptake region. Autoradiography studies confirm the uptake of radium-223, especially in the vicinity of activated osteoblasts (Suominen *et al* 2017). When mature, osteoblasts are cubic cells that wrap around the surface of the trabecular bone (Suominen *et al* 2017). Therefore, although the thickness of the endosteum was updated to 50 μ m, the radioactive source region remained 10 μ m thick.

Hence, the source region was assumed to have a uniform radium-223 uptake distribution into a 10 μ m-thick shell from the bone surface towards the bone marrow, representing the location of the activated osteoblasts. This

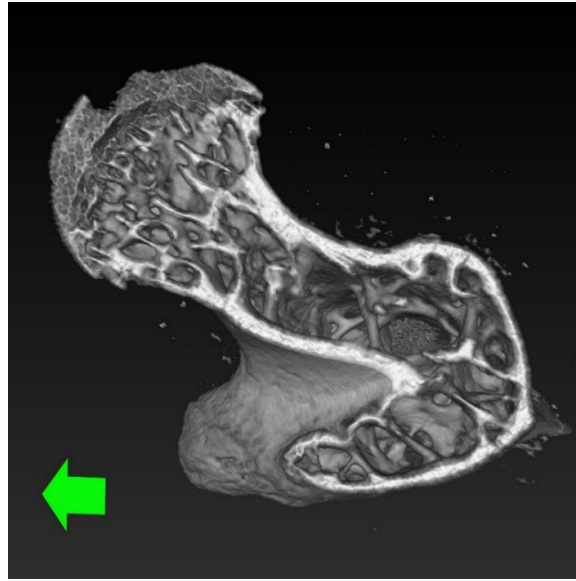


Figure 4. Micro-CT image of an antero-posterior view of a mouse femur, reconstructed by the post-processing software Avizo Fire 8.1.

work assumes instantaneous radium-223 uptake and infinitely long biological retention, according to previously published works in mice (Henriksen *et al* 2003).

2.6. Sample segmentation and source region construction

GATE simulations require a description of the volume materials as well as the source activities. The micro-CT image showed some limitations regarding the differentiation of the trabecular and cortical regions, since they differ only in the size of their pores. Thus, those regions were not distinguished and were labelled only as bone. However, this limitation does not alter the quality of the dosimetry calculations because the source region is not located in the bone. Furthermore, the only quantitative analysis in the bone region was for the short-range alpha emissions. The separation of trabecular and cortical regions should be evaluated for dosimetry analysis in which the flow of hydroxyapatite labelled with radium-223 inward to the bone or the existence of a calcified osteogenic tumour may exhibit radionuclide absorption. Similarly, the endosteal region and bone marrow could not be distinguished because it would require other techniques, such as visualization of histological sections under a microscope, as well as a micro-CT scan with higher spatial resolution.

The GATE user guide recommends that both the image and the source voxels have the same size. Thus, the image was resampled to a $10 \times 10 \times 10 \mu\text{m}^3$ voxel size to match its thickness to that of the endosteal region, where the osteoblasts are located (source). Furthermore, a nonlinear 3D median filter with kernel size $3 \times 3 \times 3$ was applied to remove noise (Kramer *et al* 2010).

Next, bone segmentation at the microscale was assessed using FCM (Chuang *et al* 2006). Clustering is an unsupervised machine learning technique used to find similarities among data points and group similar data points together (Bezdek *et al* 1999, Ross 2010). The voxels extracted from each VOI on the CT images were clustered into k partitions using the FCM algorithm. FCM uses a clustering technique in which a data set is grouped into c clusters, with each data point in the data set belonging to every cluster to a certain degree. Here, the FCM algorithm was applied to the data on a VOI basis, which, in this context, includes the whole bone. In this method, cluster number determination is an essential step of the FCM algorithm (Ross 2010), and the natural cluster number depends on image heterogeneity. We assumed that 2 (two) partitions, i.e. the bone and trabecular cavities, were sufficient to accommodate bone heterogeneity.

The FCM algorithm segments an image by iteratively optimizing parameter partitioning through minimization of the squared error objective function. The objective function J is described by:

$$J = \sum_{i=1}^N \sum_{j=1}^c u_{ji}^m d^2(f_i, v_j), m > 1.$$

Let f_i be defined as the i th voxel used for clustering, N as the total number of all voxels, v_j as the j th cluster centre, c as the number of clusters ($2cN$), u_{ji} as the degree of voxel membership, f_i as the j th cluster and m as the fuzzy coefficient. Following (Chuang *et al* 2006), m is 2 and the iterative convergence threshold ε is 1×10^{-6} ; the fuzzy membership matrix $U = [u_{ji}]$ is randomly initiated.

Furthermore, the variable $d^2(f, v_j)$ represents the distance between the data point f and cluster centre v_j . Fuzzy partitioning can be achieved by minimizing the objective function in the following iterative process. First, v_j is updated based on U and the following equation:

$$v_j^{(b)} = \frac{\sum_{i=1}^N (u_{ji}^{(b)})^m f_i}{\sum_{i=1}^N (u_{ji}^{(b)})^m}$$

where b is the iterative number. Once the cluster centre is obtained, the fuzzy membership matrix is updated based on the following equation:

$$u_{ji}^{(b+1)} = \frac{1}{\sum_{k=1}^c \left(\frac{d_{ji}}{d_{ki}} \right)^{\frac{2}{m-1}}}.$$

The iterative process is terminated on the basis of the difference between the present and previous fuzzy membership matrices. When $\|U^{(b)} - U^{(b+1)}\| < \varepsilon$, the iterative process is terminated, and the next iterative process begins with the updating of v_j . At the end of the iteration, the centroid of the cluster, representing the average values of all voxels weighted by their degree of belonging to the cluster, is obtained and used to compute the degree of relationship to each cluster for each pixel.

Next, the *defuzzification* process is performed according to the membership matrices for determining the clusters with the highest degree of membership in each voxel:

$$C_i = \arg_j [\max (u_{ji})] \forall_j, \forall_k$$

where C_i represents the classification to which the i th voxel belongs.

After the image was segmented, the bone tissue was used as an input to automatically delineate its edges at a 10 μm resolution. A 3D Sobel filter based on a first-order derivative was used to obtain the edges, following (Gonzalez and Woods 2006, Kramer *et al* 2010). This filter enabled us to create the layer representing the source in the image and the subsequent layers so that we could associate the voxel with the position inside the trabecular cavity.

2.7. Materials and density of sample regions

For the validation model and the bone sample, the elemental compositions and densities per mass of trabecular bone and active bone marrow followed the ICRP Publication 89 recommendations (Valentin 2002) for humans. The endosteum was considered active bone marrow. Therefore, 100% cellularity was assumed. The bone mineral density values for C57BL/6 mice are similar to those used for humans but are measured in units of hydroxyapatite (gHA cm^{-3}), as suggested by Halloran *et al* (2002).

2.8. Cell-based dosimetric analysis

The absorbed dose map and VOI image from GATE were fused and analysed in VV software, version 1.4 (Seroul and Sarrut 2008). Considering an absorbed dose calculation per region, the acquisition time was estimated to reach an absorbed dose of 2 Gy for alpha emissions within the VOI trabecular cavities of the femur. The absorbed dose value is close to that estimated for bone marrow during a six-cycle course of therapy using radium-223 (Lassmann and Nosske 2013) and to the reported value for possible haematologic toxicity to the bone marrow (O'Donoghue *et al* 2002).

A mask was created on the segmented image with a 10 μm -thick layer from the internal bone surface with different identifications (IDs) for the femur VOI. This thickness was chosen based on the expected size of the single osteoblast shell previously described. Thus, each ID was associated with a thickness of 10 μm from the inner layer of bone. The endosteum was assumed to be the first five layers (from 0 to 50 μm), and the source region was represented by the first layer (0 to 10 μm). This mask and the absorbed dose (or number of hits) provided by GATE were processed by a modified MATLAB® script to extract the absorbed dose (or hits) matrix for each ID and, consequently, to calculate the absorbed dose (or hits) histogram in the voxel as a function of the radial distance from the bone. The average absorbed dose in each shell in the trabecular cavities was also quantified.

3. Results and discussion

3.1. Morphological analysis of the femoral neck

Figure 5 shows the VOI of the femoral neck (a) and magnifications of the cortical and trabecular structure in this region (b) and (c).

Table 2 shows the morphological analysis calculated for this sample in CTAn software from Bruker, presented according to the recommended nomenclature (Parfitt *et al* 1987).

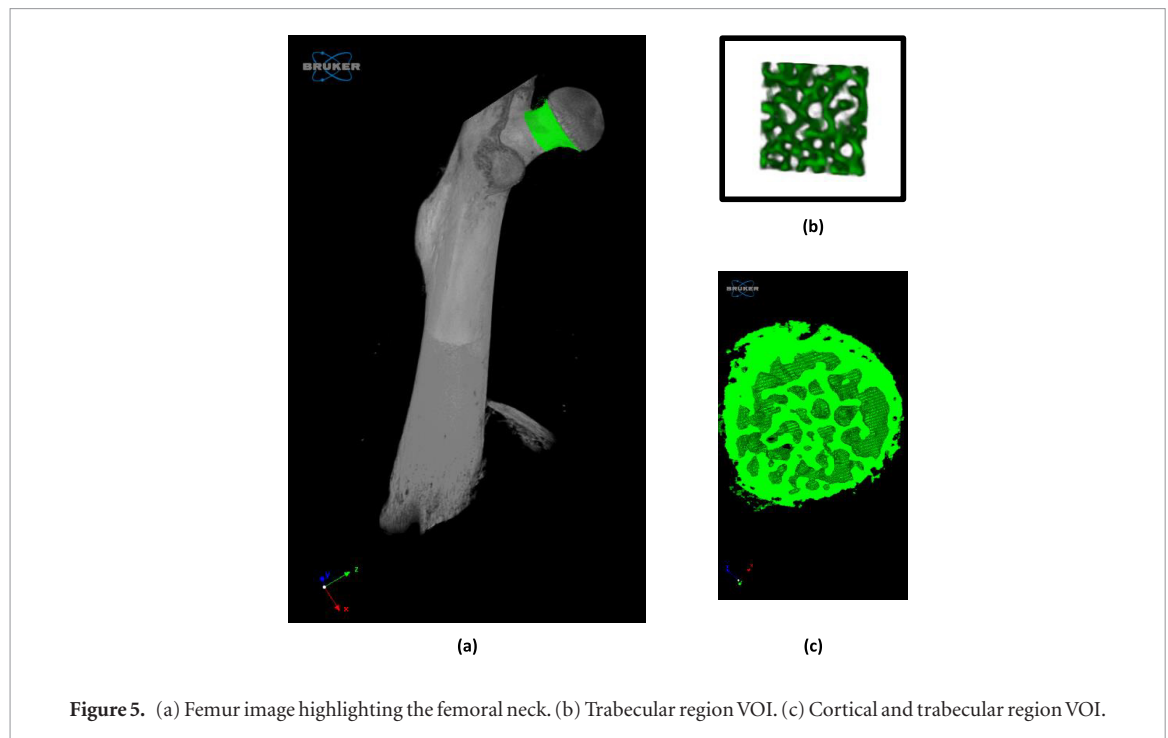


Figure 5. (a) Femur image highlighting the femoral neck. (b) Trabecular region VOI. (c) Cortical and trabecular region VOI.

3.2. Simulation validation and update

Table 3 shows the AF values for radium-223 considering endosteal region as the source region and bone marrow and ER as the target regions. AF values were calculated with GATE, according to ICRP Publications 30 and 110, for endosteal regions with thicknesses of 10 μm and 50 μm , respectively. Reference values (Hobbs *et al* 2012) are also listed. The statistical uncertainties of the AF values obtained with GATE were lower than 0.4%. AF computation was performed assuming the radium-223 decay energy to be 27.5 MeV (Henriksen *et al* 2003).

The AF value calculated with GATE, AF (BM \leftarrow ER), with the 10 μm thick endosteal region (ICRP 30), was comparable to the value reported by Hobbs (2012). For the absorbed fraction AF (ER \leftarrow ER), the values provided by GATE were larger than the value from the reference. Hobbs *et al* (2012) did not present the AF for the trabecula. Concerning the discrepancies between the results, it is worth noting that the simulation of the radium-223 decay chain in GATE describes the characteristic emission particle spectrum, while the Hobbs reference considered average energy values.

According to table 3, the AF in the bone marrow with endosteal region thickness (t_{ER}) equal to 10 μm was 40% of the value of the fraction with t_{ER} equal to 50 μm . On the other hand, the AF in the endosteal region tripled when t_{ER} changed from 10 to 50 μm . Therefore, the absorbed dose was highly concentrated in the endosteal region when its thickness follows the recommendation of ICRP Publication 110 (ICRP 2008), increasing the risk for bone cancer due to the irradiation of osteoblasts and osteoprogenitor cells. This updated thickness value resulted in a substantial change in the AF values, indicating that dosimetry studies with high-LET particles should follow the more recent recommendations.

The simulation results obtained with the physics lists *emstandard_opt3* and *emstandard_opt4* and with single and multiple scattering did not present discrepancies in the calculated AF values. Since the physics list *emstandard_opt4* is considered the most precise (Matta *et al* 2016), it was chosen for the subsequent simulations in this study.

3.3. Bone sample dosimetric analysis

Figure 6 shows the application of the automatic segmentation method FCM in the central slice of the VOI of the femoral neck. Resampling of the femur VOI to 10 μm cubic voxels resulted in 96 slices. Figure 6(a) shows the resampled central slice of this VOI. Figure 6(b) depicts this segmented slice, and figure 6(c) shows the segmented image after modifications: creation of the source layer, differentiation of the bone marrow and background, and highlighting of the bone in blue. The created 10 μm shell is the source region and is depicted in red; the remaining trabecular cavity is in yellow.

The resulting segmented VOI was used to describe the voxellized geometry of the bone structure in GATE.

Applying the physics list *emstandard_opt4*, the influence of the use of single and multiple scatterings on the average absorbed dose and the number of interactions was investigated in each segmented VOI region of the femur. Only the alpha emission was considered in this analysis because it was the main contributor to the

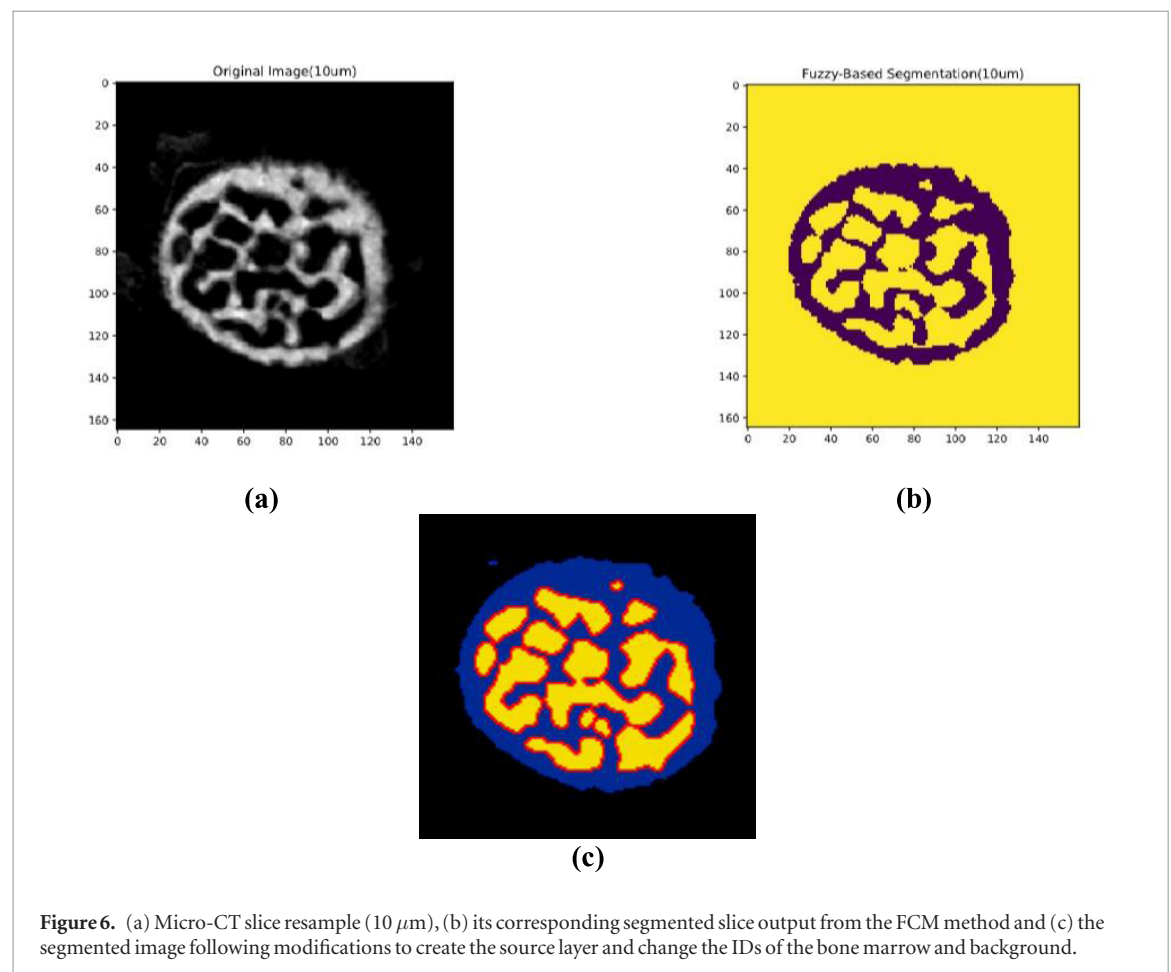
Table 2. Morphological analysis of the femoral neck.

Parameters	Femoral neck
BV/TV	0.83%
Bone surface (BS)	9.93 mm ²
Bone surface/volume ratio (BS/BV)	31.60 (mm) ⁻¹
Trabecular thickness (Tb.Th)	0.11 mm
Trabecular separation (Tb.Sp)	0.65 mm
Degree of anisotropy	1.47 (0.32)
Structure model index	1.77
Connectivity density	$1.07 \times 10^{-6} \text{ (mm}^3\text{)}^{-1}$

Table 3. GATE and reference (Hobbs *et al* (2012)) values of the absorbed fraction (AF) for radium-223 with the endosteal region (ER) as the source region and bone marrow (BM) and ER as the target regions. The endosteal region thickness (t_{ER}) values were 10 μm and 50 μm , according to ICRP Publications 30 and 110, respectively. The statistical uncertainties of the calculated GATE values were lower than 0.4%.

AF ^a	GATE		Reference
	ICRP 30 ($t_{ER} = 10 \mu\text{m}$)	ICRP 110 ($t_{ER} = 50 \mu\text{m}$)	ICRP 30 ($t_{ER} = 10 \mu\text{m}$)
AF (BM \leftarrow ER)	3.5×10^{-1}	1.4×10^{-1}	3.5×10^{-1}
AF (ER \leftarrow ER)	2.5×10^{-1}	6.8×10^{-1}	2.3×10^{-1}

^a Absorbed fraction (target \leftarrow source).



absorbed dose. The acquisition time was the same for all simulations. This time was estimated assuming an absorbed dose in the trabecular cavity of approximately 2 Gy. The results are presented in table 4.

The absorbed dose values in table 4 were in agreement within 2 (two) standard deviations and indicate a good accuracy of the multiple scattering model. In fact, the scattering model did not interfere in either AF results (table 3) or absorbed dose (table 4) values. On average, each interaction (hit) with multiple scattering activated corresponds to two interactions with single scattering. The simulation computation time using the multiple scattering

Table 4. Average absorbed dose (D) and number of interactions (# Hits) for each scattering type assuming 2 Gy at the cavities.

Region/type of scattering	Single scattering		Multiple scattering	
	D (mGy)	# hits	D (mGy)	# hits
Bone	578 ± 1	6.17×10^9	581 ± 1	3.89×10^9
Source	2939 ± 1	5.29×10^9	2937 ± 1	2.59×10^9
Trabecular cavity	1549 ± 1	4.99×10^9	1549 ± 1	2.49×10^9

process was approximately 110 h, approximately 63 h less than the computation time for the single scattering process. Nevertheless, the following simulation results were based on a single scattering model, since it provided the number of particle interactions more precisely than the multiple scattering model (table 4).

Figure 7 shows the absorbed dose map (Gy) for the voxellized image from the radium-223 decay chain in different projections. Figure 8 shows the absorbed dose map (Gy) filtered by the type of particle emission from the radium-223 decay chain. In the transaxial projection, slice 48 was chosen for its central position, slice 9 illustrates a change in the trabecular cavity size, and slice 82 (antero-posterior projection) has a representative absorbed dose distribution in relation to other slices.

As expected, the alpha emissions made the largest contribution to the absorbed dose. The beta emissions also contributed to the absorbed dose, which was slightly spread throughout the distribution map. The gamma emissions had an absorbed dose lower than 0.6 mGy (figure 8(a)). As shown in figure 8(c), the absorbed dose was concentrated near the bone surface, even when all emission contributions were considered. There were also regions where the trabecular cavity had a wider diameter (see slices 82 and 9) and, therefore, was not homogeneously compromised.

Some works (Henriksen *et al* 2003, Hobbs *et al* 2012), based on simplified geometry simulations, show that the maximum range of alpha particles do not reach the bone marrow cavity centre. It is worth noting in figures 7 and 8 that even for the mouse femoral neck, where the cavities were small and possessed a complex geometric structure, some central regions from the trabecular cavity did not receive a large enough absorbed dose to have deterministic effects on the bone marrow (2 Gy average absorbed dose). The centres of these cavities contain primary stem cells, which are the most radiosensitive because they are the least differentiated (Lord 1990, Watchman 2005).

A mask for the trabecular cavities was created to represent and quantify all the VOI voxels (3D) at the cellular level. Each layer was radially created from the bone surface to the cavity centre on 10 μm -thick transaxial projections. Figure 9 depicts two slices (48 and 9) of the fusion of the segmented image by the FCM method containing the created mask.

Using the created mask for the trabecular cavities, the average absorbed dose per layer was quantified, as were the absorbed dose and number of interactions at the cellular (or voxel) level for alpha and beta emissions. The absorbed dose values from radium-223 gamma emissions (figure 8(a)) are not shown due to their small contribution.

Figure 10(a) presents the absorbed dose histogram for each 10 μm -thick layer radially created from the bone surface. The colours referring to each position (average layer thickness for the transaxial position) are shown. Since figure 10(a) illustrates a non-parametric distribution, the median is a suitable parameter to represent the central tendency of the absorbed dose value distribution. Thus, figure 10(b) shows the medians and the interquartile intervals (error bars) characteristic of the event and the simulated geometry.

Nineteen 10 μm -thick layers were created, with few voxels in the innermost layers. Starting from the layer with a radial distance of 120 μm , no difference was observed in the histograms. The maximum absorbed dose in a single voxel was approximately 6.25 Gy. The histograms in figure 10(a) also show a pattern in absorbed dose distribution. As the distance from the layer to the internal bone surface increases, the histogram peaks diminished and shifted to the left. Moreover, the distribution became more skewed. Since the simulated geometries were irregular, the absorbed dose delivery was heterogeneous for the whole layer. The absorbed dose heterogeneity for voxels of the same layer was due to the simulation of more realistic cavities. The authors are not aware of studies of the quantification of cellular interactions using micro-CT images of the trabecular bone.

According to figure 10(b), the endosteal cells received an absorbed dose of approximately 2.2 Gy, 1.8 Gy, 1.4 Gy, 948 mGy and 566 mGy for the positions at 10 μm , 20 μm , 30 μm , 40 μm , and 50 μm from the internal bone surface, respectively. As a comparison with macroscopic quantities, the average absorbed dose was also calculated for both the 50 μm thick endosteal region and the trabecular cavity, yielding 1.7 Gy and 985 mGy, respectively. These results agreed with those from the literature regarding the absorbed dose profile at the larger cavities, namely, they were sharp until 50 μm and near zero in subsequent layers. In the smaller cavity (radius 50 μm), the difference between absorbed dose proportion of the last layers and the first layer was also similar to our results. This occurred because the geometry used here has different cavity thicknesses. The study that presents an average

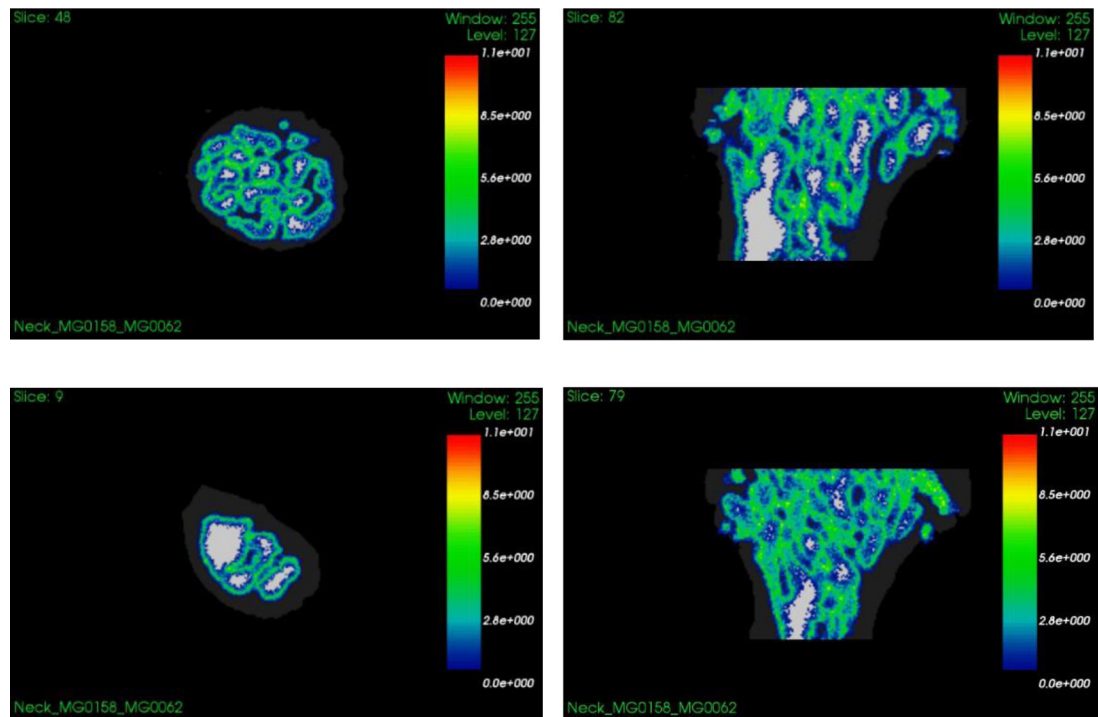


Figure 7. Absorbed dose distribution map in the femoral neck delivered by the complete radium-223 chain in different projections.

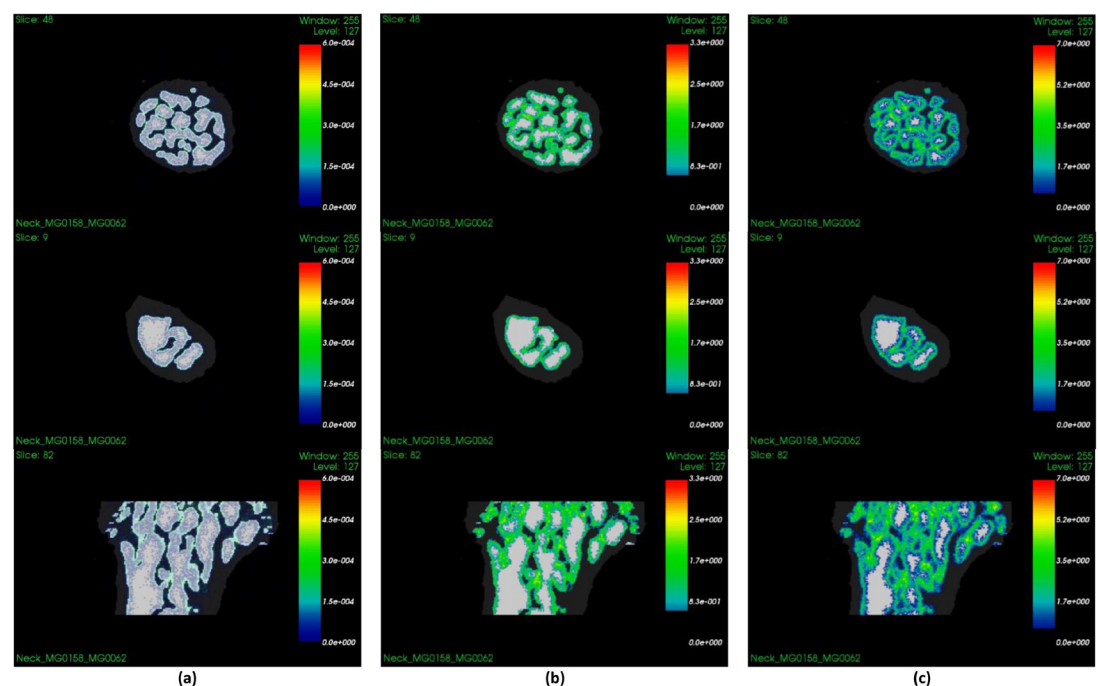


Figure 8. Absorbed dose distribution maps in the femoral neck delivered by (a) gamma emissions, (b) beta particles and (c) alpha particles for the complete radium-223 chain.

absorbed dose of 2 Gy at the cavity (Hobbs *et al* 2012) was not comparable to the present results because it uses a single sphere of radius 400 μm . Additionally, the results presented by Henriksen *et al* (2003) for the absorbed dose as a function of radial distance use cavities with radii within the range of those present in this study. However, since the simulated absorbed doses were different, a direct comparison is not possible.

Although the alpha particles delivered absorbed doses below 2 Gy at cells more than 50 μm away from the surface (figure 10), the absorbed doses in the cells of the endosteal region (osteoblasts and osteoprogenitor cells) could be associated with an increased risk of cancer induction (ICRP 2008, 2013). As there is a trend (Pacilio *et al* 2016) towards the use of higher doses in patients at the initial stage of cancer or even in younger patients, the

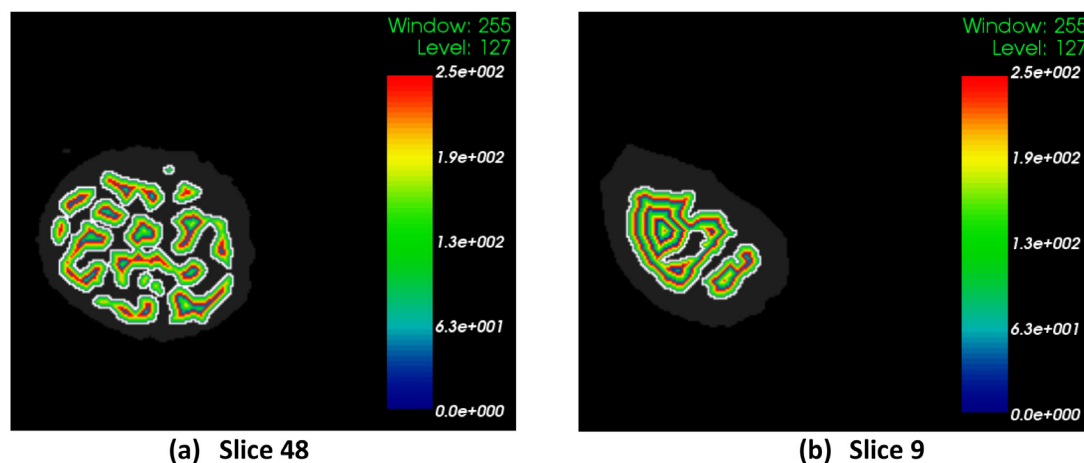


Figure 9. Fusion of the segmented image with the mask of the inner layers in the trabecular cavities visualized in VV[®] software for femoral neck slices 48 and 9.

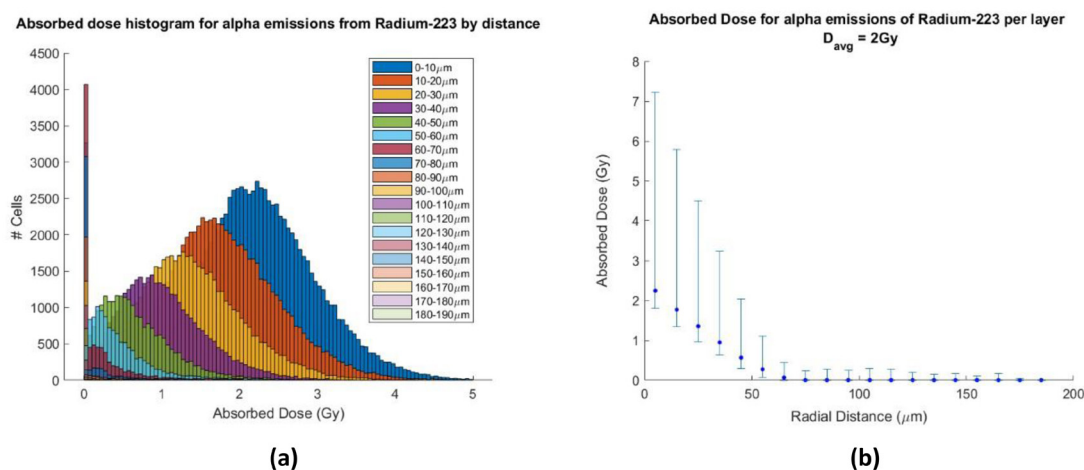


Figure 10. (a) Absorbed dose histogram (Gy) at the voxels from the trabecular cavities in the femoral neck VOI. (b) Absorbed dose (Gy) versus radial distance from the internal bone surface for alpha emissions.

quantification of the average and cellular-level absorbed doses in the endosteal region is recommended to evaluate the efficacy and risk estimation for bone cancer induction.

In order to quantify the contribution of beta emissions, the histogram and profile of the absorbed dose at the cells were plotted (figure 11) for each 10 μm thick layer radially created from the bone surface. The simulated scenario was the same as for alpha emission but with a filter for electrons.

The beta-emission histograms in figure 11(a) were similar to the alpha particle distributions but were sharper due to the shorter amplitude of the absorbed dose on the X-axis and the higher number of zero-dose voxels. In this case, the absorbed dose values of the first five layers from the internal bone surface were 1.1 Gy, 776 mGy, 542 mGy, 354 mGy, and 218 mGy, as illustrated in figure 11(b) by the median and interquartile range. The absorbed dose values at the cells corresponded to a 726 mGy average absorbed dose at the endosteum and approximately 415 mGy at the bone marrow. The contribution of alpha and beta particles represented 70.1% and 29.8% of the total absorbed dose, respectively. Summing the contributions of some cellular positions both for alpha and beta emissions, the absorbed dose at the voxel level increased to 2 Gy (see figures 10 and 11), i.e. possible damage to the cell could arise with contributions from both emissions.

Histograms of the number of interactions (hits) for both alpha and beta emissions at the cells (voxels) for each layer are depicted in figure 12 given a 2 Gy average absorbed dose for alpha emissions at the trabecular cavities of the femoral neck VOI.

This histogram has a similar pattern to the absorbed dose histograms from figures 9 and 10, with a high number of particle interactions for all layers. However, 15 370 out of a total of 310 852 cells did not undergo any interactions with alpha particles, and 15 527 cells underwent up to 20 interactions; meanwhile, for beta particles, each cell underwent at least 20 interactions.

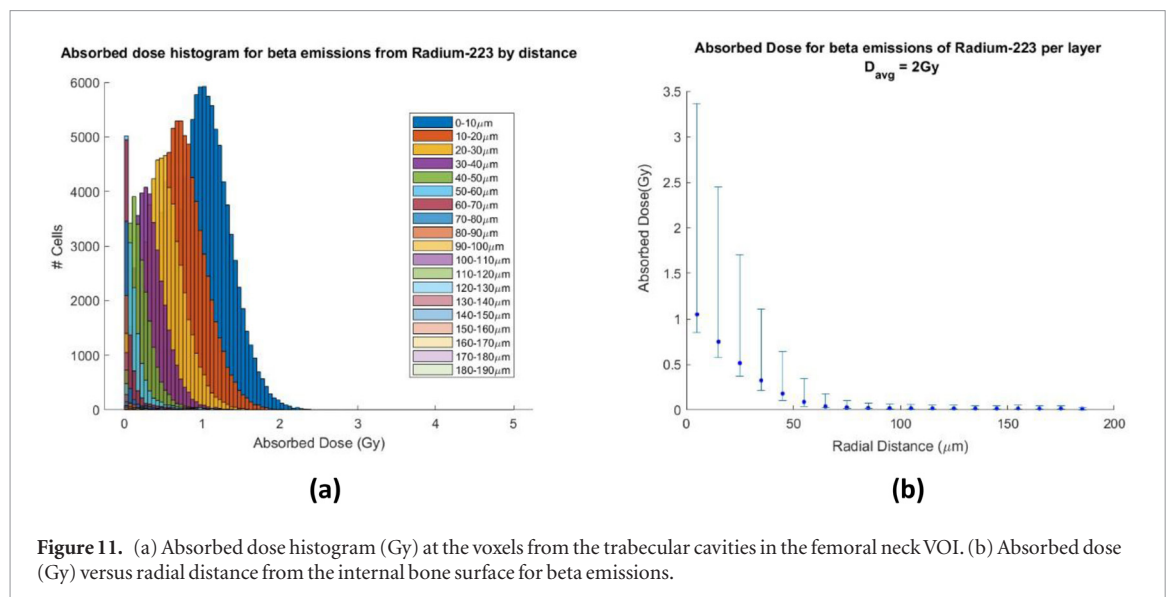


Figure 11. (a) Absorbed dose histogram (Gy) at the voxels from the trabecular cavities in the femoral neck VOI. (b) Absorbed dose (Gy) versus radial distance from the internal bone surface for beta emissions.

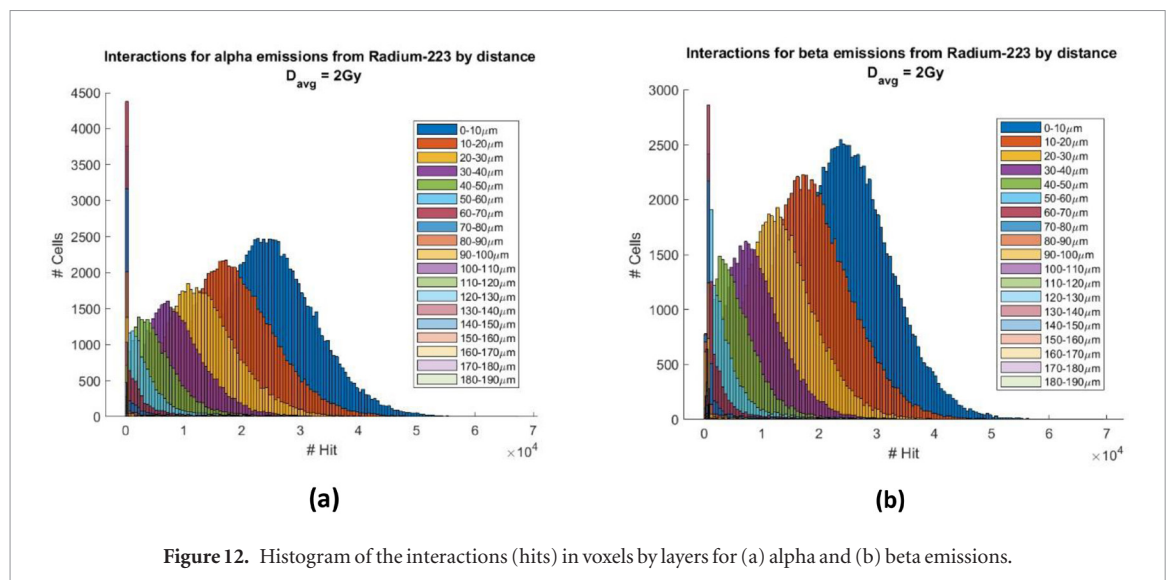


Figure 12. Histogram of the interactions (hits) in voxels by layers for (a) alpha and (b) beta emissions.

Although the 30 μm-deep layer had the largest number of voxels with absorbed doses smaller than 2 Gy (figures 10 and 11), a high number of particle interactions ($\sim 10^4$) can be observed for this layer in figure 12. The ratio of absorbed dose to hit ratio in the voxels as a function of the radial distance was verified in terms of the mean and median values and plotted in figure 13 for alpha (a) and beta emissions (b). The dose-to-hit ratio was calculated by dividing the dose value at each voxel by its corresponding number of hits.

The ratio of absorbed dose to hits increased smoothly with radial distance for alpha particles (up to approximately 1.28×10^{-4} Gy/hit) and gradually decreased for beta emissions (reaching of approximately 3.44×10^{-5} Gy/hit). The median values were similar to the mean values, diverging after 60 μm for the alpha particles and in the interval of 60 to 100 μm for beta particles. The divergence between the mean and median values was more pronounced for the beta particles than for the alpha particles.

The absorbed dose at the bone marrow in humans was estimated to be approximately 1.5 Gy for a complete treatment with radium-223 (6 cycles) (Lassmann and Nosske 2013). Therefore, the use of 2 Gy for the femoral neck VOI from the trabecular cavity of a mouse femur in this study corresponds to the estimated therapy value in humans. Moreover, since this six-cycle therapy in mouse ended with a large quantity of voxels with absorbed dose values below 1 Gy, administration of radium for human patients can likely be increased based on these results.

As a rule, alpha particle treatment efficacy is associated with their capacity to, even with few interactions, generate a double-strand DNA break or indirect effects to the DNA through damaging the cytoplasm (McDevitt *et al* 1998). However, this work and another (Gholami *et al* 2015) show that the energy per interaction of these particles should also be evaluated. For instance, the hits histogram alone may suggest high toxicity at the cavity cells. Nevertheless, previous studies in mice injected with 0.4 kBq g^{-1} did not reveal any sign of acute toxicity (Henriksen *et al* 2003). On the other hand, the results from Larsen *et al* (2006) showed a pronounced depletion of osteoblasts and osteocytes in trabecular bone at the metaphysis and a substantial depletion of haematopoietic cells

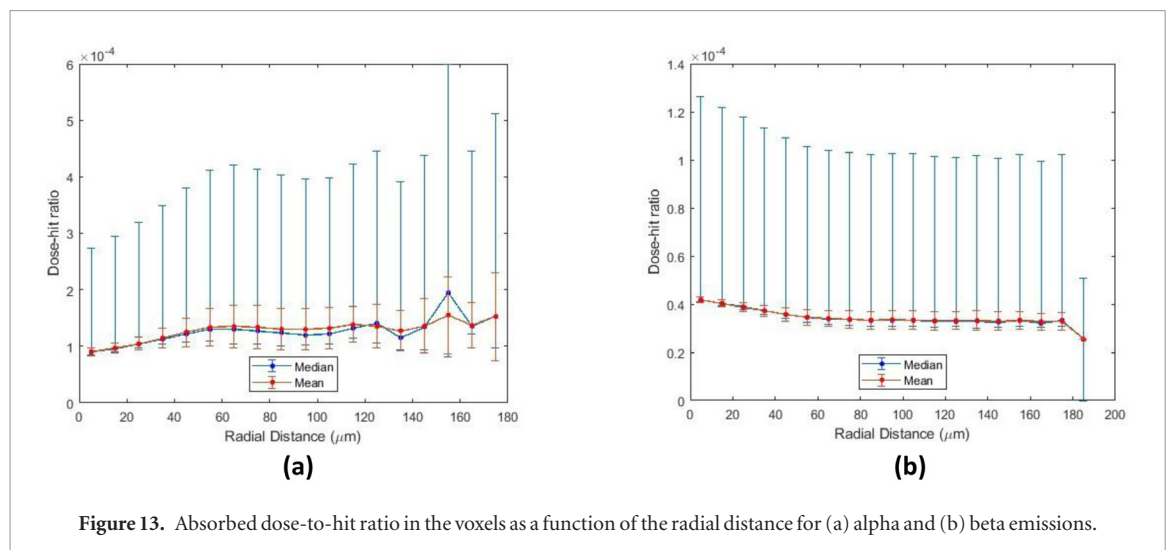


Figure 13. Absorbed dose-to-hit ratio in the voxels as a function of the radial distance for (a) alpha and (b) beta emissions.

at the metaphysis and epiphysis. Nevertheless, since the primary goal of this research was to study radium-223 radiotoxicity, the specific dose administered ($>1250 \text{ kBq kg}^{-1}$) to the mice was much higher than that used in therapy.

Thus, while some studies found a better absorbed dose-effect relationship, both the absorbed dose and number of hits should be quantified to evaluate the best parameter in the attribution of effects induced by radiation in treatments with high LET particles.

The present study does not consider the replacement of cells that undergo apoptosis due to absorbed doses or hit; it also does not consider the flux of hydroxyapatite labelled with radium-223 inward to the bone. Moreover, the skeletal tissue considered in this study was from a healthy mouse. A calcified osteogenic tumour could exhibit radionuclide absorption (Henriksen *et al* 2003).

4. Conclusion

This work presents a cell-based dosimetry model using GATE validated with a simplified geometry description of a mouse bone structure. The bone structure description was improved in a more realistic fashion using a micro-CT image.

The proposed segmentation method was used to successfully separate the irregular geometry of the bone image and to create a mask to represent the source region. As the segment method is an unsupervised learning method, i.e. automatic and operator independent, it can be extended to analyse bone at any site.

The absorbed dose at the deterministic level was near the bone surface, with smaller absorbed doses in the central bone marrow region. Therefore, the absorbed dose distribution at the bone marrow cavity using a simplified geometry (concentric spheres) described in a previous work was reproducible in the micro-CT image.

Absorbed doses from beta emissions increased the toxic potential of radium-223 in cells near the bone surface.

The numbers of alpha- and beta-particle interactions in the cells were on the order of 10^4 . However, most of the cells did not receive absorbed dose values above the level that typically results in deterministic effects on the bone marrow. Concerning the absorbed dose rate per hit at the voxel level, the reported values were below the levels that typically lead to deterministic effects on the bone marrow.

Finally, this study may be used to aid in the correlating the absorbed dose with the effects of radiation in *ex vivo* animal studies using Monte Carlo calculations and micro-CT images. Further work should analyse the track pattern of each particle to better correlate the effects of alpha particle interactions on bone metastases.

Acknowledgments

We would like to thank DSc Thiago Barboza, visiting researcher from the Laboratory of Marking of Cells and Molecules (LMCM), Department of Radiology (HUCFF/UFRJ), for preparing the bone sample.

Likewise, we also thank Olga Oliveira from the Nuclear Instrumentation Laboratory (NIL) at PEN/COPPE/UFRJ for her support in the micro-CT scanning of the bone sample and the corresponding morphological analysis.

This study was financed in part by the Brazilian National Council for Scientific and Technological Development (CNPq)-Finance Code: 141894/2014-8.

References

- Abou D S, Ulmert D, Doucet M, Hobbs R F, Riddle R C and Thorek D L J 2016 Whole-body and microenvironmental localization of radium-223 in naïve and mouse models of prostate cancer metastasis *J. Natl. Cancer Inst.* **108** djv380
- Agostinelli S et al 2003 Geant4—a simulation toolkit *Nucl. Instruments Methods Phys. Res. A* **506** 250–303
- Allison J et al 2016 Recent developments in Geant4 *Nucl. Instrum. Methods Phys. Res. A* **835** 186–225
- Bezdek J C, Keller J, Krisnapuram R and Pal N R 1999 *Fuzzy Models and Algorithms for Pattern Recognition and Image Processing* vol 4 (Boston, MA: Springer)
- Carvalho S M, Costa A P M, Ramos C D, Castelo J H M, Brunetto S Q and Bonifácio D A B 2018 Influence of the {SPECT} calibration source position on the absorbed dose calculation for ^{131}I -{NaI} therapy using {GATE} simulations *J. Radiol. Prot.* **38** 1284–92
- Chuang K-S, Tzeng H-L, Chen S, Wu J and Chen T-J 2006 Fuzzy c-means clustering with spatial information for image segmentation *Comput. Med. Imaging Graph.* **30** 9–15
- Costa G C A, Bonifácio D A B, Sarrut D, Cajgfinger T and Bardiès M 2017 Optimization of GATE simulations for whole-body planar scintigraphic acquisitions using the XCAT male phantom with ^{177}Lu -DOTATATE biokinetics in a Siemens Symbia T2 *Phys. Medica* **42** 292–7
- Costa G C A, de Sa L V and Bonifacio D A B 2015 Application of GATE/Geant4 for internal dosimetry using male ICRP reference voxel phantom by specific absorbed fractions calculations for photon irradiation *Biomed. Phys. Eng. Express* **1** 45201
- Dant J T, Richardson R B and Nie L H 2013 Monte Carlo simulation of age-dependent radiation dose from alpha- and beta-emitting radionuclides to critical trabecular bone and bone marrow targets *Phys. Med. Biol.* **58** 3301–19
- Elbast M et al 2012 Microdosimetry of alpha particles for simple and 3D voxelised geometries using MCNPX and Geant4 Monte Carlo codes *Radiat. Prot. Dos.* **150** 342–9
- Geyer A M, Schwarz B C, Hobbs R F, Sgouros G and Bolch W E 2017a Quantitative impact of changes in marrow cellularity, skeletal size, and bone mineral density on active marrow dosimetry based upon a reference model *Med. Phys.* **44** 272–83
- Geyer A M, Schwarz B C, O'Reilly S E, Hobbs R F, Sgouros G and Bolch W E 2017b Depth-dependent concentrations of hematopoietic stem cells in the adult skeleton: Implications for active marrow dosimetry *Med. Phys.* **44** 747–61
- Gholami Y, Zhu X, Fulton R, Meikle S, El-Fakhri G and Kuncic Z 2015 Stochastic simulation of radium-223 dichloride therapy at the sub-cellular level *Phys. Med. Biol.* **60** 6087–96
- Gonzalez R C and Woods R E 2006 *Digital Image Processing* 3rd edn (Upper Saddle River, NJ: Prentice-Hall)
- Halloran B P, Ferguson V L, Simske S J, Burghardt A, Venton L L and Majumdar S 2002 Changes in bone structure and mass with advancing age in the male C57BL/6J mouse *J. Bone Miner. Res.* **17** 1044–50
- Hauf S, Kuster M, Batič M, Bell Z W, Hoffmann D H H, Lang P M, Neff S, Pia M G, Weidenspointner G and Zoglauer A 2013a Radioactive decays in Geant4 *IEEE Trans. Nucl. Sci.* **60** 2966–83
- Hauf S, Kuster M, Batič M, Bell Z W, Hoffmann D H H, Lang P M, Neff S, Pia M G, Weidenspointner G and Zoglauer A 2013b Validation of Geant4-based radioactive decay simulation *IEEE Trans. Nucl. Sci.* **60** 2984–97
- Henriksen G, Fisher D R, Roeske J C, Bruland Ø S and Larsen R H 2003 Targeting of Osseous Sites with alpha-emitting ^{223}Ra : comparison with the beta-emitter ^{89}Sr in Mice *J. Nucl. Med.* **44** 252–9
- Hobbs R F, Baechler S, Fu D X, Esaías C, Pomper M G, Ambinder R F and Sgouros G 2011 A model of cellular dosimetry for macroscopic tumors in radiopharmaceutical therapy *Med. Phys.* **38** 2892–903
- Hobbs R F, Song H, Watchman C J, Bolch W E, Aksnes A K, Ramdahl T, Flux G D and Sgouros G 2012 A bone marrow toxicity model for ^{223}Ra alpha-emitter radiopharmaceutical therapy *Phys. Med. Biol.* **57** 3207–22
- Hough M, Johnson P, Rajon D, Jokisch D, Lee C and Bolch W 2011 An image-based skeletal dosimetry model for the ICRP reference adult male—internal electron sources *Phys. Med. Biol.* **56** 2309–46
- ICRP 1979 ICRP Publication 30 (Part 1): Limits for intakes of radionuclides by workers *Ann. ICRP* **2** (3–4)
- ICRP 1995 ICRP Publication 70: Basic anatomical and physiological data for use in radiological protection: the skeleton *Ann. ICRP* **25** (2) ([https://www.icrp.org/publication.asp?id=ICRP Publication 70](https://www.icrp.org/publication.asp?id=ICRP%20Publication%2070) <https://www.icrp.org/publication.asp?id=ICRP%20Publication%2070>)
- ICRP 2009 ICRP Publication 110: Adult reference computational phantoms *Ann. ICRP* **39** (2) 1–165
- ICRP 2015 ICRP Publication 130 (Part 1): Occupational intakes of radionuclides *Ann. ICRP* **44** (2)
- Jan S et al 2011 GATE V6: A major enhancement of the GATE simulation platform enabling modelling of CT and radiotherapy *Phys. Med. Biol.* **56** 881
- Kassis A 2002 Radiobiology aspects and radionuclide selection criteria in cancer therapy *Therapeutic Applications of Monte Carlo Calculations in Nuclear Medicine (Series in Medical Physics and Biomedical Engineering)* ed H Zaidi and G Sgouros (London: Taylor and Francis) pp 175–201
- Klutz P G et al 2014 Dichloride injection: U.S. Food and Drug Administration Drug approval summary *Clin. Cancer Res.* **20** 9–14
- Kramer R, Cassola V F, Khoury H J, Vieira J W, de Lima V J M and Brown K R 2010 FASH and MASH: female and male adult human phantoms based on polygon mesh surfaces: II. Dosimetric calculations *Phys. Med. Biol.* **55** 163
- Kramer R, Cassola V F, Khoury H J, Vieira J W, de Melo Lima V J and Brown K R 2009 FASH and MASH: female and male adult human phantoms based on polygon mesh surfaces: II. Dosimetric calculations *Phys. Med. Biol.* **55** 163–89
- Kramer R, Cassola V F, Vieira J W, Khoury H J, De Oliveira Lira C A B and Brown K R 2012 Skeletal dosimetry based on μCT images of trabecular bone: Update and comparisons *Phys. Med. Biol.* **57** 3995–4021
- Kramer R, Khoury H J, Vieira J W and Kawrakow I 2006 Skeletal dosimetry in the MAX06 and the FAX06 phantoms for external exposure to photons based on vertebral 3D-microCT images *Phys. Med. Biol.* **51** 6265–89
- Kramer R, Khoury H J, Vieira J W and Kawrakow I 2007 Skeletal dosimetry for external exposure to photons based on μCT images of spongiosa from different bone sites *Phys. Med. Biol.* **52** 6697–716
- Larsen R H, Saxtorph H, Skydsgaard M, Borrebaek J, Jonasdottir T J, Brulanda O S, Klastrup S, Harling R and Ramdahl T 2006 Radiotoxicity of the alpha-emitting bone-seeker ^{223}Ra injected intravenously into mice: histology, clinical chemistry and hematology *In Vivo* **20** 325–32
- Lassmann M and Nosske D 2013 Dosimetry of ^{223}Ra -chloride: dose to normal organs and tissues *Eur. J. Nucl. Med. Mol. Imaging* **40** 207–12
- Lien L M E, Tvedt B and Heinrich D 2015 Treatment of castration-resistant prostate cancer and bone metastases with radium-223 dichloride *Int. J. Urol. Nurs.* **9** 3–13
- Lord B I 1990 The architecture of bone marrow cell populations *Int. J. Cell Cloning* **8** 317–31
- Martin M J 2013 Nuclear data sheets for $A = 152$ *Nucl. Data Sheets* **114** 1497–847
- Matta A, Morfouace P, de Séréville N, Flavigny F, Labiche M and Shearman R 2016 {NPTTool}: a simulation and analysis framework for low-energy nuclear physics experiments *J. Phys. G Nucl. Part. Phys.* **43** A5113

- McDevitt M R, Sgouros G, Finn R D, Humm J L, Jurcic J G, Larson S M and Scheinberg D A 1998 Radioimmunotherapy with alpha-emitting nuclides *Eur. J. Nucl. Med.* **25** 1341–51
- Mínguez P, de Iturriaga A G, Fernández I L and Rodeño E 2018a Detección y cuantificación de la captación de ^{223}Ra en metástasis óseas en pacientes con carcinoma de próstata resistente a la castración con vistas a la determinación de la dosis absorbida en dichas metástasis *Rev. Esp. Med. Nucl. Imagen Mol.* **37** 20–7
- Mínguez P, Roeske J C, Mínguez R, De Iturriaga A G and Rodeño E 2018b Comparison of microdosimetry-based absorbed doses to control tumours and clinically obtained tumour absorbed doses in treatments with ^{223}Ra *Phys. Med. Biol.* **63** 045005
- Mitchell D G, Rao V M, Dalinka M, Spritzer C E, Axel L, Geffer W, Kricun M, Steinberg M E and Kressel H Y 1986 Hematopoietic and fatty bone marrow distribution in the normal and ischemic hip: new observations with 1.5-T MR imaging *Radiology* **161** 199–202
- Nilsson S *et al* 2007 Bone-targeted radium-223 in symptomatic, hormone-refractory prostate cancer: a randomised, multicentre, placebo-controlled phase II study *Lancet Oncol.* **8** 587–94
- Nilsson S, Larsen R H, Fosså S D, Balteskard L, Borch K W, Westlin J E, Salberg S and Bruland O S 2005 First clinical experience with α -emitting radium-223 in the treatment of skeletal metastases *Clin. Cancer Res.* **11** 4451–9
- O'Donoghue J A *et al* 2002 Hematologic toxicity in radioimmunotherapy: dose-response relationships for I-131 labeled antibody therapy *Cancer Biother. Radiopharma.* **17** 435–43
- Pacilio M *et al* 2016 Dosimetry of bone metastases in targeted radionuclide therapy with alpha-emitting ^{223}Ra -dichloride *Eur. J. Nucl. Med. Mol. Imaging* **43** 21–33
- Pafundi D, Lee C, Watchman C, Bourke V, Aris J, Shagina N, Harrison J, Fell T and Bolch W 2009 An image-based skeletal tissue model for the ICRP reference newborn *Phys. Med. Biol.* **54** 4497–531
- Pafundi D, Lee C, Watchman C, Bourke V, Aris J and Bolch W 2009 Image-based skeletal dosimetry models for the ICRP reference pediatric series *J. Nucl. Med.* **50** (suppl.2) 267
- Pafundi D, Rajon D, Jokisch D, Lee C and Bolch W 2010 An image-based skeletal dosimetry model for the ICRP reference newborn–internal electron sources *Phys. Med. Biol.* **55** 1785–1814
- Pandit-Taskar N, Larson S M and Carrasquillo J A 2014 Bone-seeking radiopharmaceuticals for treatment of osseous metastases, part 1 a therapy with ^{223}Ra -dichloride *J. Nucl. Med.* **55** 268–74
- Parfitt A M, Drezner M K, Glorieux F H, Kanis J A, Malluche H, Meunier P J, Ott S M and Recker R R 1987 Bone histomorphometry: Standardization of nomenclature, symbols, and units: report of the asbmr histomorphometry nomenclature committee *J. Bone Miner. Res.* **2** 595–610
- Parker C *et al* 2013 Alpha Emitter Radium-223 and Survival in Metastatic Prostate Cancer *N. Engl. J. Med.* **369** 213–23
- Ross T J 2010 *Fuzzy Logic with Engineering Applications* (New York: Wiley) (<https://doi.org/10.1002/9781119994374>)
- Sarrut D *et al* 2014 A review of the use and potential of the GATE Monte Carlo simulation code for radiation therapy and dosimetry applications *Med. Phys.* **41** 64301
- Sgouros G 2008 Alpha-particles for targeted therapy *Adv. Drug Deliv. Rev.* **60** 1402–6
- Sgouros G, Roeske J C, McDevitt M R, Palm S, Allen B J, Fisher D R, Brill A B, Song H, Howell R W and Akabani G 2010 MIRD pamphlet No. 22 (Abridged): radiobiology and Dosimetry of particle emitters for targeted radionuclide therapy *J. Nucl. Med.* **51** 311–28
- Suominen M I *et al* 2017 Radium-223 inhibits osseous prostate cancer growth by dual targeting of cancer cells and bone microenvironment in mouse models *Clin. Cancer Res.* **23** 4335–46
- Valentin J 2002 Basic anatomical and physiological data for use in radiological protection: reference values: ICRP Publication 89 *Ann. ICRP* **32** 1–277
- Van't Hof R J 2012 Analysis of bone architecture in rodents using microcomputed tomography *Bone Research Protocols* ed M H Helfrich and S H Ralston (Totowa, NJ: Humana Press) pp 461–76
- Vieira S C, Lustosa A M L, Barbosa C N B, Teixeira J M R, de Brito L X E, Soares L F M and Ferreira M A T 2012 *Oncologia Básica* (Teresina, PI, BRA: Fundação Quixote)
- Watchman C J 2005 Skeletal Dosimetry Models for Alpha-Particles for Use in Molecular Radiotherapy *Dissertation* (University of Florida) (http://etd.fcla.edu/UF/UFE0012165/watchman_c.pdf)
- Watchman C J, Bourke V A, Lyon J R, Knowlton A E, Butler S L, Grier D D, Wingard J R, Braylan R C and Bolch W E 2007 Spatial distribution of blood vessels and CD34⁺ hematopoietic stem and progenitor cells within the marrow cavities of human cancellous bone *J. Nucl. Med.* **48** 645–54